

# Direct observation of crack arrest after bridge notch failure: A strategy to increase statistics and reduce FIB-artifacts in micro-cantilever testing

Yinxia Zhang<sup>a</sup>, Matthias Bartosik<sup>b</sup>, Steffen Brinckmann<sup>c</sup>, Subin Lee<sup>a,\*</sup>, Christoph Kirchlechner<sup>a</sup>

<sup>a</sup> Institute for Applied Materials, Karlsruhe Institute of Technology, D-76344 Eggenstein-Leopoldshafen, Germany

<sup>b</sup> Department of Materials Science, Montanuniversität Leoben, A-8700 Leoben, Austria

<sup>c</sup> Microstructure and Properties of Materials (IEK-2), Forschungszentrum Jülich, D-52425 Jülich, Germany

## ARTICLE INFO

### Keywords:

Micro-cantilevers  
Fracture toughness  
Bridge notch  
Geometry influence

## ABSTRACT

Focused ion beam (FIB) milling has been widely used to prepare micron-sized specimens for micromechanical testing, however, at the same time, unavoidable artifacts originating from the Ga<sup>+</sup> ion beam might alter the obtained mechanical properties. Using a bridge notch geometry, which can promote the formation of a sharp natural crack after bridge-failure rather than creating a comparably blunt FIB notch was proposed as a strategy to reduce FIB-induced artifacts more than a decade ago. Even though bridge-failure is widely assumed and predicted by finite element method (FEM) simulations, it has never been observed and quantified experimentally. This study presents the first experimental observation of bridge notch failure and crack arrest before the entire through-thickness main notch (after crack arrest) propagates, which is possible by designing thin bridges and using a stiff experimental setup with superior load resolution. Consequently, we obtained up to three corresponding fracture toughness values from one bending cantilever and significantly less scattered data. Using previously reported geometry correction factors calculated by FEM, the fracture toughness estimated from the bridge-failure was compared with the one from the failure of the main through-thickness notch in CrN/AlN multi-layered and CrN hard coatings.

## 1. Introduction

In recent years, there have been significant advances in the design of hard protective coatings that have yielded improved mechanical properties [1]. In hard coating applications, several micrometers thick coatings deposited on the substrate determine the service life of the component. Determining and optimizing their mechanical properties, for example, fracture toughness, has become one of the most challenging tasks since the conventional approaches cannot be applied and there is no standardized procedure to evaluate the fracture toughness at the micro/nano scale [2]. The most widely used experimental method for assessing fracture toughness  $K_{Ic}$  at a small length scale is the single micro-cantilever fracture test [3–5], because it is relatively easy to fabricate samples with a well-defined geometry.

In most cases, micro-cantilevers and their pre-notch are fabricated using Ga<sup>+</sup> focused ion beam (FIB) milling. There are different types of pre-notches for single micro-cantilever beam geometry, for instance, a chevron notch [6], a through-thickness notch [7], and a bridge notch [8]. Compared to the simple and well-defined geometry of a cantilever

with a through-thickness notch, it is difficult to determine the crack length in cantilevers with chevron notches during the test and to maintain the symmetry of the chevron notch during FIB milling. In the case of through-thickness notches, it is easier to calculate fracture toughness from the experiment because of its well-defined geometry, however, the higher milling rate of the FIB at the side of the cantilevers, so-called “over-fibbing” results in a curved notch front rather than a straight front. Furthermore, the stress-field around the over-fibbed notch is significantly more complicated compared to that of an ideal through-thickness notch.

Besides the over-fibbed notch geometry of a micro-cantilever, FIB-induced artifacts, for example, Ga<sup>+</sup> implantation [9], knock-on damage [10], FIB-induced crystal defects [11,12], residual stresses [13], a finite notch root radius [8,14] and re-deposition [15], strongly affect the fracture toughness values measured by micro fracture experiment. Although FIB milling can produce sharp notches at the desired location with high spatial resolution, it has a certain root radius, typically around 10 nm [8], which is larger than that of natural cracks or fatigue cracks. There are alternative geometries for micro fracture tests, such as

\* Corresponding author.

E-mail address: [subin.lee@kit.edu](mailto:subin.lee@kit.edu) (S. Lee).

<https://doi.org/10.1016/j.matdes.2023.112188>

Received 2 March 2023; Received in revised form 18 July 2023; Accepted 21 July 2023

Available online 22 July 2023

0264-1275/© 2023 The Authors. Published by Elsevier Ltd. This is an open access article under the CC BY-NC-ND license (<http://creativecommons.org/licenses/by-nc-nd/4.0/>).

clamped beam bending geometry [16], which can promote stable crack propagation thus the sample fails by a natural crack, however, there are more complications and limitations in this geometry, for instance, notch alignment. Another approach to circumvent the Ga<sup>+</sup> FIB artifacts is using FIB with different ion species [17], or optimizing FIB milling conditions [18]. For instance, He from helium ion beam milling (HIM) does not show any chemical interactions with the sample [19] and also offers a smaller beam size, resulting in smaller notch root radius [20]. HIM can also be used to fabricate micro cantilevers, however, the milling speed is much slower than Ga<sup>+</sup> FIB milling [21].

One of the approaches to reduce the FIB-induced cantilever side effects is using a bridge notch. As soon as the thin bridge fails, an atomically sharp crack will be nucleated and propagate leading to the complete failure of the cantilever [8]. This method has been proven effective in various material systems such as carbide hard-coatings [22], silicon oxide thin films [8], or intermetallic phases [23]. The advantage of this geometry is that it can create a natural crack which is less affected by FIB damage, so that it is possible to measure materials' inherent properties. However, to the best of our knowledge, bridge failure had not been experimentally observed.

The computation of a new geometry factor is required to assess the fracture toughness from a single cantilever with a bridge notch. Brinckmann et al. [24] computed this geometry factor and related it to the geometry factor of a through-thickness one by defining a correction factor. Based on this correction factor and the geometry factor of a through-thickness notch, the local stress intensity at the bridge notch can be estimated.

In this study, we present the first observation of crack propagation and crack arrest at the bridge notch before the final fracture of a single cantilever in CrN/AlN multi-layered and CrN monolithic hard coatings. The quantification of the fracture toughness from the bridge-failure shows good correlation (less than 10% deviation) to the one calculated from the failure of the main through-thickness notch after the bridge failure, in other words crack arrests.

## 2. Materials and methods

### 2.1. Thin coating preparation

Two different coatings were grown on Si (100) substrates by unbalanced reactive magnetron sputtering: monolithic CrN with a thickness of 1.46 μm and a CrN/AlN multi-layered coating with a total thickness of 1.88 μm. The CrN/AlN multi-layered coating consisted of alternating layers of approximately 4 nm CrN and 2 nm AlN. The coatings were prepared in an AJA ATC-1800 ultra-high vacuum deposition system equipped with one Cr (purity 99.95%) and one Al (purity 99.99%) target, which both had a three-inch diameter. The targets were powered in pulsed DC mode with a pulse frequency of 100 kHz and a pause of 1 μs. A time-averaged power of 300 W and 500 W was applied to the Cr and Al target materials, respectively. The coatings were grown in a mixed N<sub>2</sub>/Ar (12 sccm / 8 sccm flow rate ratio) gas atmosphere at a total gas pressure of 0.2 Pa. A DC bias voltage of -70 V was applied to the substrates during coating growth to ensure the formation of a dense coating morphology. While the deposition parameters were kept constant throughout the deposition process, mechanical shutters under computer control opened and closed at regular time intervals to create the multilayer structure (in the case of the CrN/AlN multi-layered coating).

Prior to the deposition, the Si (100) substrates (7 × 20 × 0.38 mm<sup>3</sup>) were pre-cleaned in an acetone- or ethanol-filled ultrasonic bath for at least 5 min in each, before they were clamped on the substrate holder and transferred to the vacuum chamber in the load-lock system. The base pressure in the vacuum chamber was below 3 × 10<sup>-6</sup> mbar. After thermal cleaning of the substrates at 550 °C for 30 min, the substrates were ion etched for 5–10 min at 500 °C in pure Ar atmosphere and the targets were sputter-cleaned under the closed shutters for 5 min using

the same parameters as later used during the deposition process, first in pure Ar gas and then in mixed N<sub>2</sub>/Ar gas atmosphere. The substrates rotated constantly with a rotation frequency of about 0.5 Hz.

### 2.2. Fabrication of micro-cantilevers

Before producing cantilevers using FIB, the silicon substrates of both CrN/AlN multi-layered and CrN hard coatings were etched using a 30 wt % potassium hydroxide (KOH) solution for 30 min at 60 °C to obtain 20 μm long freestanding film segments. Then, the cantilevers were prepared by FIB milling (Crossbeam 550L, Zeiss) at 30 kV in 3 steps; rough milling with 3nA, intermediate milling with 700 pA, and fine milling with 50 pA probe current. Notches were fabricated with a 20 pA current and 1.0 μs dwell time to have a straight notch front without noticeable FIB re-deposition. The geometry of cantilevers is shown in Fig. 1;  $L$  is the distance between the loading position and the notch,  $H$  is the distance between the base of the cantilever and the notch,  $B$  is the cantilever width,  $b$  is the notch width,  $W$  is the cantilever thickness,  $a$  is the notch depth. The  $a/W$  ratios are between 0.2 and 0.3. The nominal width  $B$  of the cantilever was about 1.9 μm for CrN/AlN multi-layered hard coatings and 1.5 μm for CrN hard coatings, and the nominal ratios of  $H:L:W:B$  are 1:5:1:1. The width of ligaments (or bridges) next to the notch,  $b$ , was kept as small as possible, with a ratio of  $b/B$  of 0.92 which implies that each bridge has a relative width of 4% with respect to the cantilever width.

### 2.3. In situ SEM mechanical testing

*In situ* micromechanical fracture experiments were conducted to determine the fracture toughness of the hard coatings inside an SEM (Merlin Gemini II, Zeiss). A Hysitron PI 89 NG SEM PicoIndenter (Bruker) equipped with a 10 μm wide diamond wedge tip (Synton-MDP AG) was used in displacement-controlled mode with a displacement rate of 5 nm/s. The low load transducer of the PI 89 NG was used, which has a maximum load of 10 mN and noise floor of 0.4 μN.

### 2.4. Data analysis

The analytical solution for the conditional fracture toughness  $K_{I_Q, ref}$  in single cantilever bending tests under loads gives [8]:

$$K_{I_Q, ref} = \frac{FL}{BW^{3/2}} f_{Matoy} \left( \frac{a}{W} \right) \quad (1)$$

where  $F$  is the load at fracture, and  $f_{Matoy} \left( \frac{a}{W} \right)$  is a geometry shape factor for an ideally straight through-thickness notch proposed by Matoy et al. [8] which is described as below.

$$f_{Matoy} \left( \frac{a}{W} \right) = 1.46 + 24.36(a/W) - 47.21(a/W)^2 + 75.18(a/W)^3 \quad (2)$$

In this study, we use bridge notches that do not have a straight initial crack front (see Fig. 1, right). According to the FEM simulations of Brinckmann et al. [24], the relative ratio between the stress intensity at the top of the bridges and the one at the center of the notch depends on the geometry of the bridges, which is described by the aforementioned correction factor. Using the correction factor, the conditional fracture toughness can be calculated from a micro-cantilever with a bridge notch. A detailed evaluation of the stress intensity factors in the different cantilever sections follows in Section 3.3.

Note that the conditional fracture toughness  $K_{I_Q, ref}$  as calculated from Eq. (1) can be considered as fracture toughness  $K_{Ic}$  for the samples investigated in this study.

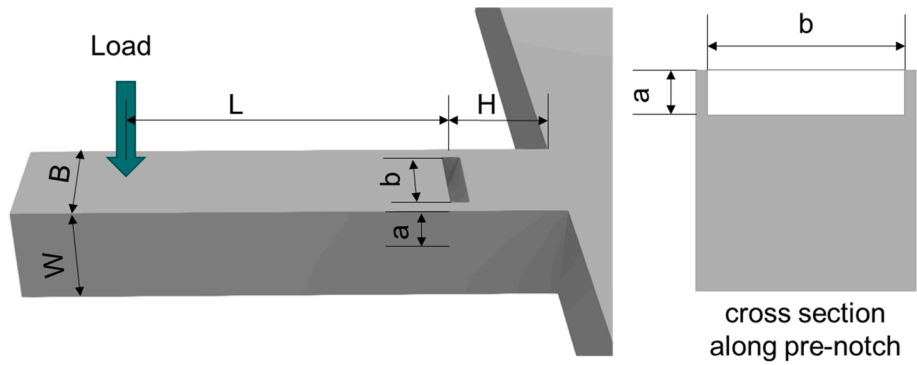


Fig. 1. Geometry of a bridge notch single cantilever.

### 3. Results

#### 3.1. Direct observation of material bridge-failure

Fig. 2a shows a SEM image of a representative CrN/AlN multi-layered micro-cantilever with a bridge notch before deformation. The load–displacement curve shows elastic loading in the beginning and three discontinuous points, denoted as B1, B2, and C (Fig. 2b). By image-frame analysis of the *in situ* SEM video, it is found that B1 and B2 correspond to the failure of the bridges as shown in Fig. 2d and e, respectively (see Supplementary Video S1). Compared to the image before the bridge-failure (Fig. 2c), arrested cracks are clearly visible after bridge failure, as pointed out by the white arrows in Fig. 2d and e. Once the bridges break, the cantilever stiffness is reduced by 10% in average, and this stiffness reduction leads to a load drop at B1 and B2 as

the displacement is constant. The length of the arrested crack in Fig. 2e is measured to be 630 nm which is a little deeper than the depth of the FIB-notch which is 575 nm. Fig. 2f shows an SEM image of the fractured surface; the CrN/AlN multi-layered coating has a dense morphology, and the columnar grain structure is visible. However, any noticeable features at the bridges which might originate from the crack arrest cannot be detected. For the fracture toughness evaluation in the following sections, the geometry and depth of the notch were measured from the fracture surface images.

#### 3.2. Cumulative distribution of the maximum load

Similar experiments were performed on 11 cantilevers from CrN/AlN multilayer hard coatings. For each test, the bridge failure and subsequently crack arrest before the final fracture were observed. And Fig. 3

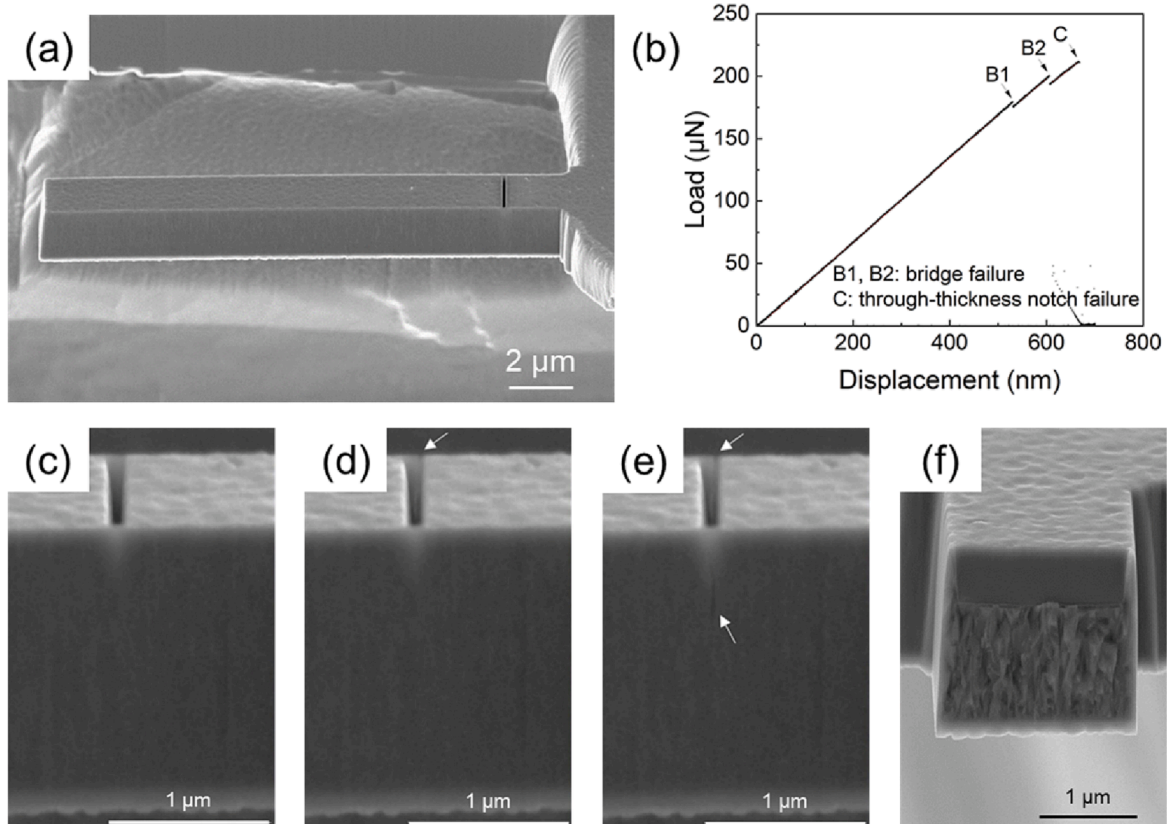


Fig. 2. (a) Free-standing CrN/AlN multi-layered hard coating cantilever; (b) load–displacement curve showing elastic region and three discontinuous points. B1 and B2 are the bridge-failure points, and C is the cantilever fracture point; (c) SEM image of the cantilever before the bridge-failure; (d) SEM image showing failure of one of the bridges when the load reaches to B1; (e) SEM image at B2 showing the failure of the other bridge; (f) fracture surface of the cantilever after point C.

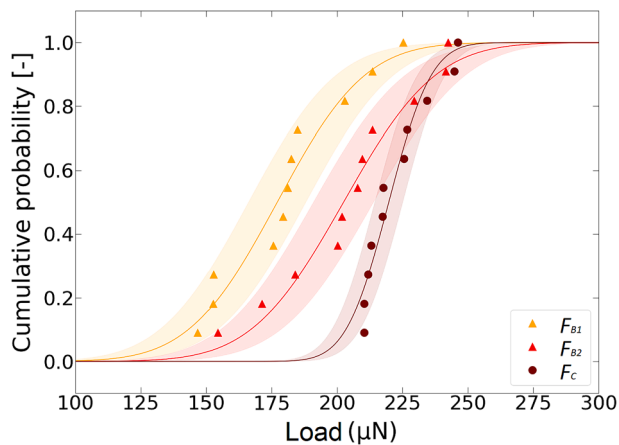


Fig. 3. The normal cumulative distribution of load measured at B1, B2 and C for 11 CrN/AlN multi-layered cantilevers. The shade bands represent 95% confidence intervals.

shows the cumulative distribution function of the load drops, the maximum load at B1, B2, and C point correspond to  $F_{B1}$ ,  $F_{B2}$ , and  $F_C$ , respectively. We fit those data with a normal cumulative distribution function (CDF). The shades represent a 95% confidence interval.  $F_{B1}$ ,  $F_{B2}$ , and  $F_C$  mean load is 177.1  $\mu\text{N}$ , 202.5  $\mu\text{N}$ , and 219.8  $\mu\text{N}$ , and the standard deviation is 26.4  $\mu\text{N}$ , 27.7  $\mu\text{N}$ , and 12.8  $\mu\text{N}$ , respectively.

The key findings are reflected in the cumulative probability curve: (i) The force for the complete cantilever failure,  $F_C$ , shows much less scatter compared to  $F_{B1}$  and  $F_{B2}$ , as the standard deviation is less than half of that of  $F_{B1}$  and  $F_{B2}$ . A possible scenario is that the complete failure of the cantilever is driven by natural cracks which are formed by bridge failure, thus  $F_C$  is less susceptible to FIB artifacts, for example, FIB damage and notch radius. (ii) The variation of the distribution in  $F_{B1}$  and  $F_{B2}$  are comparable. This suggests that the earlier bridge failure at B1, does not affect the second bridge failure event.

In most of cases, we observed two distinct load drops for each bridge failure at points B1 and B2. In rare cases, B1 and B2 occurred at the same load. Due to a possible asymmetry of the bridge shape on either side e.g. due to slight differences in bridge geometry, redeposition at the FIB-notch, different grain boundaries at the two bridges, and *et cetera*, B1 and B2 typically do not occur at exactly the same load. As soon as both bridges failed (see region after B2 in the load–displacement curve (Fig. 2b)), the notch can be regarded as a through-thickness notch with a sharp natural crack at both sides (Fig. 2d). The stress intensity, in this case, can be described by equation (1), which means that the fracture toughness obtained from  $F_C$  at point C is  $K_{Ic} = K_{IQ, ref. C}$ .

### 3.3. Cumulative distribution of the $K_{Ic}$

From the maximum force before the fracture of bridges and cantilevers,  $F_{B1}$ ,  $F_{B2}$ , and  $F_C$ , the critical stress intensity factors were calculated. In the case of the final fracture,  $F_C$ , we assumed a through-thickness notch although the exact geometry of the FIB-notch and the natural crack after the breaking of the bridges is more complex. In the case of bridge failure, we used a correction factor,  $f_{corr}$ , proposed by Brinckmann et al. [24], which predicts the stress intensity at the top side of the bridge with respect to the one at the center of the FIB-notch. Then, we can calculate the bridge failure toughness  $K_{Ic}^*$  using the same geometry factor for the cantilever by Matoy et al. [8] and correcting the relative ratio between stress intensity at the top of the bridge. It can be expressed as,

$$K_{Ic}^* = K_{IQ, ref. B} / f_{corr} \quad (3)$$

$$K_{Ic}^* = \frac{F_B L}{BW^{3/2}} f_{Matoy} \left( \frac{a}{W} \right) / f_{corr} \quad (4)$$

where  $F_B$  is the load ( $F_{B1}$  and  $F_{B2}$ ) at points B1 or B2 in the load–displacement curve at bridge failure.  $f_{corr}$  depends on the geometry of the bridge notch, i.e.  $a/W$  ratio as well as  $1-b/B$ . A detailed description of  $f_{corr}$  is followed in Section 4.1 and also in the Ref. [24]. After crack arrest, the notch can be regarded as a through-thickness notch with a sharp natural crack. Finally, we calculated the through-thickness notch fracture toughness  $K_{Ic}$  from the through-thickness notch after crack arrest, and the bridge notch toughness  $K_{Ic}^*$  from the bridge failure using equations (1) and (4) as shown in Fig. 4a.  $K_{Ic}$  shows slightly higher fracture toughness while the scatter is less compared to  $K_{Ic}^*$ . The same experiment and analysis were conducted on a different material system, CrN monolithic coating, of which results are shown in Fig. 4b. The similar trends can be seen, for example, a higher through-thickness fracture toughness  $K_{Ic}$  from the complete fracture of the cantilever but with less deviation, compared to the bridge notch fracture toughness  $K_{Ic}^*$ .

The mean fracture toughness ( $K_{Ic}^*$  and  $K_{Ic}$ ) for the CrN/AlN multi-layered hard coating is  $2.5 \pm 0.4 \text{ MPa}\cdot\text{m}^{1/2}$  and  $2.7 \pm 0.1 \text{ MPa}\cdot\text{m}^{1/2}$ , respectively. For the CrN hard coating, the mean fracture toughness is  $2.6 \pm 0.4 \text{ MPa}\cdot\text{m}^{1/2}$  and  $2.8 \pm 0.2 \text{ MPa}\cdot\text{m}^{1/2}$ , respectively. The smaller scatters in the through-thickness notch fracture toughness  $K_{Ic}$  could originate from the sharper natural cracks after the bridge failure and fewer FIB artifacts.

The reason for the shift of the cumulative distribution can generally be analyzed by plotting the ratios of  $K_{Ic}/K_{Ic}^*$ , calculated for both hard coatings separately (see Fig. 5). Even though the two sample systems had slightly different cantilever dimensions due to different coating thicknesses, the cumulative distribution of the ratio between  $K_{Ic}$  and  $K_{Ic}^*$  is almost identical. The mean of  $K_{Ic}/K_{Ic}^*$  is  $1.07 \pm 0.15$  and  $1.07 \pm 0.17$  for CrN hard coating and CrN/AlN multi-layered hard coatings, respectively. Consequently, the fracture toughness measured from the final fracture of the cantilever is 7% higher than that measured from the bridge failures. The possible reasons are discussed in Section 4.3.

## 4. Discussion

Matoy and co-workers [8] proposed the bridge notch geometry in order to form a natural crack in small scale cantilevers, which is less prone to FIB artifacts. Nevertheless, to the best of our knowledge, the intended sequence of bridge-failure, crack propagation of a sharp crack in the bridges, crack arrest, and final fracture of the micro-cantilever has never been experimentally reported before. In this section, we will first discuss the prerequisites for crack arrest in micro-cantilevers. Subsequently, we will discuss differences between the obtained fracture toughness at bridge-failure and at final fracture, differences in their scatter and finally on implications for the small scale testing community.

### 4.1. How to promote crack arrest?

In bridge notch cantilevers, fracture always initiates at the top inner corner of the bridge notch [24], where the stress intensity is highest. To observe subsequent crack arrest, the stress intensity at the bridge top needs to be larger than the stress intensity in the later formed through-thickness notch at the same displacement (or load, depending on the intrinsic behavior of the testing device). Using FEM modeling, Brinckmann and co-workers [24] mapped the ratio of the stress intensity of bridge notches and the one of through-thickness notches (see Fig. 6). This ratio strongly depends on the bridge notch geometry, i.e. on the  $a/W$  ratio as well as on the relative size of the bridge notch ( $1-b/B$ ). Stress intensity ratios larger than 1 would result in crack propagation without crack arrest because the stress intensity at the through-thickness notch would already exceed the critical value in the event of the bridge-failure.

On the other hand, when the stress intensity ratio  $f_{corr}$  (as in Fig. 6) is smaller than 1, the crack will start from the top side of the bridge because of higher stress intensity, and arrest near the FIB-notch root. It is because the stress intensity at the through-thickness notch (after crack

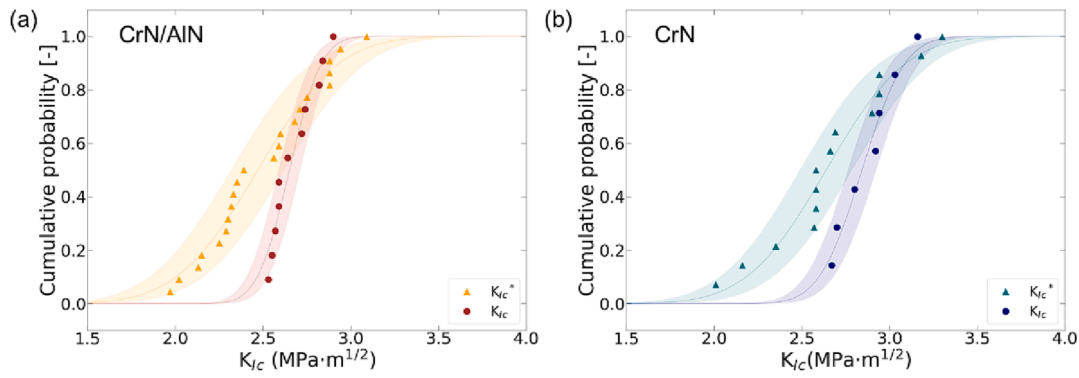


Fig. 4. The cumulative distribution functions of the bridge notch fracture toughness  $K_{Ic}^*$  and the through-thickness notch fracture toughness  $K_{Ic}$  for (a) CrN/AlN multi-layered and (b) CrN hard coatings.

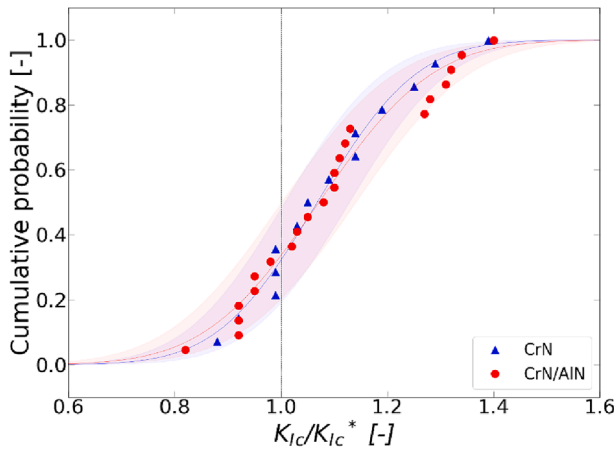


Fig. 5. The cumulative distribution function of  $K_{Ic}/K_{Ic}^*$  for the CrN hard coating and the CrN/AlN multi-layered hard coating.

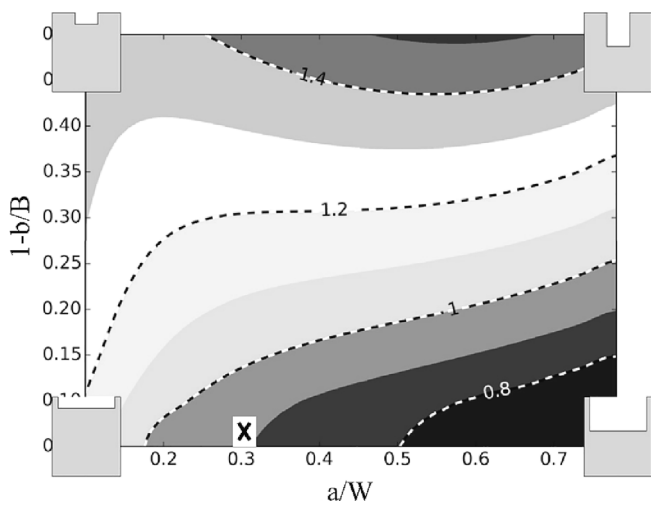


Fig. 6. Stress intensity factor in the absence of a bridge (according to the reference equation (1)) divided by the average stress intensity top half of the bridge.  $a/W$  is the ratio of the reference crack length and the cantilever thickness.  $1-b/B$  is the representation of the width of two bridges. The white rectangle with an X indicates the geometry chosen for cantilevers investigated in this study. Reproduced with permission from Brinckmann et al. [24].

arrest) is smaller than the one at the bridge part, therefore a load increase is required to propagate the crack further. To summarize, bridge notch geometries in the lower right corner of Fig. 6 promote crack arrest

while geometries in the upper left corner show continuous crack propagation and do not allow for the measurement of B1 and B2. Generally, to observe crack arrest, an  $a/W$  ratio higher than 0.2 is required and notches with very thin bridges are recommended (see Fig. 6).

The bridge geometry for the presented cantilevers is around  $a/W = 0.3$  and  $(1-b/B) = 0.07$ , which is shown by the black cross on the white rectangle in Fig. 6 resulting  $f_{corr}$  of  $\sim 0.9$ . Therefore, crack initiation at the bridge top and crack arrest after forming a through-thickness notch is expected and observed. It shall be noted that the sensor noise of less-sensitive indenter systems might hide the load drops caused by bridge-failure (points B1 and B2 in Fig. 2b). In our case, the average load drops at the bridge failure was a few  $\mu N$ .

#### 4.2. Computing multiple values for the fracture toughness based on crack arrest

There are two important implications of the bridge failure. Firstly, as previously mentioned, the natural cracks from the bridge failure significantly reduce scatters in the  $K_{Ic}$  improving accuracy of the data. But also, two additional fracture toughness values can be measured for each failure of the bridges. As micro mechanical testing is always subjected to an experimental scatter due to its sensitivity to local inhomogeneous of the microstructure, a statistical analysis is required. Therefore, two additional data points from a single experiment can help to improve the statistics thus the accuracy of the results from micro-cantilever fracture experiments.

To obtain multiple fracture toughness values from one cantilever, the position of the crack initiation needs to be correlated to the load at the onset of crack propagation to compute the correct stress intensity. As stated above, in bridge notches crack always initiates at the inner top corner of the bridge notch [24], as also observed in our experiments. The bridge notch fracture toughness  $K_{Ic}^*$  can therefore be obtained from equation (4) using the load  $F_{B1}$  and  $F_{B2}$ . Subsequently, crack arrest after bridge-failure forms a through-thickness notch (with two natural cracks at the side and the FIB-milled notch in the center), at which the final fracture occurs. The through-thickness notch fulfils the geometric requirements assumed in the FEM-based stress intensity calculations from Matoy et al. [8], and therefore, the through-thickness notch fracture toughness  $K_{Ic}$  can be calculated based on equation (1) and the load at final fracture,  $F_C$ .

#### 4.3. Possible reasons for differences in $K_{Ic}$ and $K_{Ic}^*$

The collective assessment of  $K_{Ic}$  and  $K_{Ic}^*$  reveals quantitative differences in the bridge notch fracture toughness and the through-thickness notch fracture toughness (see Fig. 5). The toughness obtained at the final fracture is 7% higher than the one obtained from bridge-failure observed from two different material systems (Fig. 5). Two main sources for these discrepancies are identified:

- (i) The local stress intensity factor as calculated from FEM models does not match the real one due to the geometry of the real sample.
- (ii) The material in the thin bridges is altered by the Ga<sup>+</sup> ion beam differently than in the sharp crack being present after crack arrest.

The FEM-based stress intensity calculations assume a vertical bridge notch with sharp corners [24]. In contrast, due to the small dimensions of the bridges which are typically less than 100 nm, a certain edge-rounding occurs, and FIB taper forms. Both effects would reduce the stress intensity in the real cantilever with respect to the ideal one modeled in FEM. Therefore, while the effect of geometric imperfections of the bridge notch is indisputable, it cannot explain the lower bridge notch fracture toughness as observed in our experiments (see Fig. 4 and Fig. 5).

Consequently, we argue that the FIB-damage in the material bridges is the main reason for the observed discrepancy. At bridge-failure, stress localizes at the top region of the bridge which is most prone to FIB milling effects, because the Ga<sup>+</sup> ion damage is expected to propagate tens of nanometers into the sample [12]. In contrast, the arrested crack which gives rise to the final fracture is a naturally formed, sharp-crack far from the region associated with FIB damages. For most materials, we assume that FIB damage results in embrittlement, rather than toughening, which would be in line with our results presented in Fig. 5.

Let us finally note that the crack driving load in a FIB-milled through-thickness notch (shown in the Fig. 3d in Ref. [24]) is largest in the sample center, where plane strain conditions are present. In this region, we expect a FIB-milled notch to have many different FIB artifacts, such as a finite notch root radius, FIB-induced crystal defects, residual stresses and *et cetera*. However, due to the slight advance of our natural crack (the surface crack is slightly longer than the FIB-milled pre-notch) and its superior sharpness, we speculate that the final fracture occurs from the two sharp cracks at the side of the specimen and not in the FIB-affected center of the notch, then the natural cracks propagate to the center of the specimen.

#### 4.4. Reasons for the increased scatter of $K_{Ic}^*$ compared to $K_{Ic}$

It is noted that the fracture toughness from bridge-failure shows substantially more scatter than the one from the newly formed through-thickness notch (compare the behavior of  $K_{Ic}$  and  $K_{Ic}^*$  in Fig. 4). We address this increased scatter by imperfections of the top region of the bridge notch: unavoidable FIB taper angle and corner rounding (see Section 4.3) result in a non-ideal bridge geometry (see Fig. 2f) that is not fully reproducible from one experiment to the other. These bridge geometry deviations are one reason for the increased scatter of the fracture toughness obtained by bridge-failure.

We believe that another possible reason is the relatively low material volume subjected to high stress intensities compared to the final through-thickness notch: while in bridge-failure we essentially see two points of high stress intensity (at the inner corner of the bridge, see [24]), the entire through-thickness notch is subjected to high stress intensities with small variations along the notch. Even when the final cracking initiates from the natural sharp cracks at the side of the specimens only, the volume being subjected to high stress intensities is substantially larger than in the two hot spots in the case of the bridge notch. The small area subjected to high stress intensities gives rise to a large scatter, as well-understood from weakest link statistics in ceramic materials [25].

#### 4.5. Implications for the FIB-based measurement of micro-cantilever fracture toughness

The observation of crack arrest after crack initiation at the bridge notch has at least two implications for the measurement of micro-

cantilever fracture toughness.

- 1) The strategy of forming a natural crack based on the bridge notch geometry, as proposed by Matoy et al. [8], is well-suited to reduce the effect of FIB-damage. Our results indicate that the toughness in a naturally formed crack is larger than the one obtained from crack initiation at the FIB-affected regions. Please note that this argument will only hold for knock-on damage, for example, the formation of stacking faults or dislocations [26], typically observed tens of nanometers from the surface [12], but does not hold for materials exhibiting extensive Ga<sup>+</sup> segregation to interfaces. For example, liquid metal embrittlement by Ga in Al is a fast process and even a small amount of implanted Ga atoms will segregate at grain boundaries far from the milled area and will change the mechanical properties of Al samples [12].
- 2) To obtain a valid estimation of the fracture toughness by bridge notch cantilevers, the location of crack initiation needs to be identified, because the stress intensity at the bridge notch and the through-thickness notch varies strongly [24]. If bridge-failure (B1 and B2 in Fig. 2) and final fracture (C in Fig. 2) can be observed *in situ* and in the load–displacement curve, the correct geometry factors can be used with confidence. In all other cases, it remains unclear if the bridge failed at the maximum load or the sharp crack gave rise to final failure. Consequently, if the imaging resolution of the *in situ* device, the load resolution of the indenter or its stiffness prevents an identification of the points B1, B2 and C, it is recommended to target bridge geometries with  $f_{corr}$  close to but smaller than 1, because the stress intensities at the bridge and the through-thickness notch after bridge failure are identical. To directly observe the bridge-failure and measure the corresponding load at the event, a  $f_{corr}$  smaller than 1 is recommended because it allows for the observation of a natural crack without / with less FIB artifacts.

## 5. Conclusions

Within this work, the fracture toughness of two different hard coatings was assessed by designing very thin bridge notches in a micro-cantilever using an *in situ* SEM indenter with high stiffness and low noise. The following conclusions can be drawn:

- The first experimental observation of cracking at the bridge notch during single cantilever bending tests on multi-layered CrN/AlN hard coatings and CrN hard coatings is presented.
- The through-thickness notch (after crack arrest) fracture of the cantilever occurs at a naturally sharp crack and therefore is less prone to FIB-milling artifacts.
- Up to three fracture toughness values were obtained from a single experiment: two bridge notch fracture toughness values from the bridge-failure and one through-thickness notch fracture toughness from the final cantilever fracture. The toughness values obtained from bridge-failure are, on average, 7% lower than the ones obtained from the final fracture of the cantilever, which may be due to the non-perfect matching of the FEM model and FIB artifacts.
- Recommendations for the testing strategy and the cantilever geometry are provided. For a direct observation of bridge failure and the measurement of the corresponding load, a  $f_{corr}$  close to but less than 1 is required. This ensures that the maximum load occurs at the final failure of the through-thickness notch after crack arrest.

## Declaration of Competing Interest

The authors declare that they have no known competing financial interests or personal relationships that could have appeared to influence the work reported in this paper.

## Data availability

Data will be made available on request.

## Acknowledgments

This research was funded within the framework of the DACH program by the national funding agencies: Austrian Science Fund (FWF) [I4720] and German Research Foundation (DFG) [436506789]. The authors thank M. T. Becker for the film deposition.

## Appendix A. Supplementary data

Supplementary data to this article can be found online at <https://doi.org/10.1016/j.matdes.2023.112188>.

## References

- [1] P.H. Mayrhofer, C. Mitterer, L. Hultman, H. Clemens, Microstructural design of hard coatings, *Prog. Mater. Sci.* 51 (8) (2006) 1032–1114, <https://doi.org/10.1016/j.pmatsci.2006.02.002>.
- [2] A. Riedl, R. Daniel, M. Stefanelli, T. Schöberl, O. Kolednik, C. Mitterer, J. Keckes, A novel approach for determining fracture toughness of hard coatings on the micrometer scale, *Scr. Mater.* 67 (7–8) (2012) 708–711, <https://doi.org/10.1016/j.scriptamat.2012.06.034>.
- [3] J. Ast, M. Ghidelli, K. Durst, M. Göken, M. Sebastiani, A.M. Korsunsky, A review of experimental approaches to fracture toughness evaluation at the micro-scale, *Mater. Des.* 173 (2019), 107762, <https://doi.org/10.1016/j.matdes.2019.107762>.
- [4] G. Dehm, B.N. Jaya, R. Raghavan, C. Kirchlechner, Overview on micro- and nanomechanical testing: New insights in interface plasticity and fracture at small length scales, *Acta Mater.* 142 (2018) 248–282, <https://doi.org/10.1016/j.actamat.2017.06.019>.
- [5] D. Di Maio, S. Roberts, Measuring fracture toughness of coatings using focused-ion-beam-machined microbeams, *J. Mater. Res.* 20 (2) (2005) 299–302, <https://doi.org/10.1557/JMR.2005.0048>.
- [6] K. Kishida, T. Maruyama, H. Matsunoshita, T. Fukuyama, H. Inui, Micropillar compression deformation of single crystals of Mo<sub>5</sub>SiB<sub>2</sub> with the tetragonal D81 structure, *Acta Mater.* 159 (2018) 416–428, <https://doi.org/10.1016/j.actamat.2018.08.048>.
- [7] S. Gabel, B. Merle, E. Bitzek, M. Göken, A new method for microscale cyclic crack growth characterization from notched microcantilevers and application to single crystalline tungsten and a metallic glass, *J. Mater. Res.* 37 (12) (2022) 2061–2072, <https://doi.org/10.1557/s43578-022-00618-x>.
- [8] K. Matoy, H. Schönherr, T. Detzel, T. Schöberl, R. Pippan, C. Motz, G. Dehm, A comparative micro-cantilever study of the mechanical behavior of silicon based passivation films, *Thin Solid Films* 518 (1) (2009) 247–256, <https://doi.org/10.1016/j.tsf.2009.07.143>.
- [9] E. Salvati, L. Brandt, C. Papadaki, H. Zhang, S. Mousavi, D. Wermeille, A. Korsunsky, Nanoscale structural damage due to focused ion beam milling of silicon with Ga ions, *Mater. Lett.* 213 (2018) 346–349, <https://doi.org/10.1016/j.matlet.2017.11.043>.
- [10] T.L. Matteson, S.W. Schwarz, E.C. Houge, B.W. Kempshall, L.A. Giannuzzi, Electron backscattering diffraction investigation of focused ion beam surfaces, *J. Electron. Mater.* 31 (1) (2002) 33–39, <https://doi.org/10.1007/s11664-002-0169-5>.
- [11] S. Lee, J. Jeong, Y. Kim, S.M. Han, D. Kiener, S.H. Oh, FIB-induced dislocations in Al submicron pillars: Annihilation by thermal annealing and effects on deformation behavior, *Acta Mater.* 110 (2016) 283–294, <https://doi.org/10.1016/j.actamat.2016.03.017>.
- [12] D. Kiener, C. Motz, M. Rester, M. Jenko, G. Dehm, FIB damage of Cu and possible consequences for miniaturized mechanical tests, *Mater. Sci. Eng. A* 459 (1–2) (2007) 262–272, <https://doi.org/10.1016/j.msea.2007.01.046>.
- [13] A. Norton, S. Falco, N. Young, J. Severs, R. Todd, Microcantilever investigation of fracture toughness and subcritical crack growth on the scale of the microstructure in Al<sub>2</sub>O<sub>3</sub>, *J. Eur. Ceram. Soc.* 35 (16) (2015) 4521–4533, <https://doi.org/10.1016/j.jeurceramsoc.2015.08.023>.
- [14] Y. Liao, M. Gruber, H. Lukic, S. Chen, S. Megremis, Fracture toughness of zirconia with a nanometer size notch fabricated using focused ion beam milling, *J. Biomed. Mater. Res. B Appl. Biomater.* 108 (8) (2020) 3323–3330, <https://doi.org/10.1002/jbm.b.34668>.
- [15] S. Rajsiri, B.W. Kempshall, S.M. Schwarz, L.A. Giannuzzi, FIB Damage in Silicon: Amorphization or Redeposition? *Microsc. Microanal.* 8 (S02) (2002) 50–51, <https://doi.org/10.1017/S1431927602101577>.
- [16] B.N. Jaya, C. Kirchlechner, G. Dehm, Can microscale fracture tests provide reliable fracture toughness values? A case study in silicon, *J. Mater. Res.* 30 (5) (2015) 686–698, <https://doi.org/10.1557/jmr.2015.2>.
- [17] C.M. Lauener, L. Petho, M. Chen, Y. Xiao, J. Michler, J.M. Wheeler, Fracture of Silicon: Influence of rate, positioning accuracy, FIB machining, and elevated temperatures on toughness measured by pillar indentation splitting, *Mater. Des.* 142 (2018) 340–349, <https://doi.org/10.1016/j.matdes.2018.01.015>.
- [18] J.P. Best, J. Zechner, J.M. Wheeler, R. Schoepfner, M. Morstein, J. Michler, Small-scale fracture toughness of ceramic thin films: the effects of specimen geometry, ion beam notching and high temperature on chromium nitride toughness evaluation, *Phil. Mag.* 96 (32–34) (2016) 3552–3569, <https://doi.org/10.1080/14786435.2016.1223891>.
- [19] D. Cohen-Tanugi, N. Yao, Superior imaging resolution in scanning helium-ion microscopy: A look at beam-sample interactions, *J. Appl. Phys.* 104(6) (2008) 063504, doi: 10.1063/1.2976299.
- [20] H. Wu, L.A. Stern, D. Xia, D. Ferranti, B. Thompson, K.L. Klein, C.M. Gonzalez, P. D. Rack, Focused helium ion beam deposited low resistivity cobalt metal lines with 10 nm resolution: implications for advanced circuit editing, *J. Mater. Sci. Mater. Electron.* 25 (2) (2014) 587–595, <https://doi.org/10.1007/s10854-013-1522-6>.
- [21] F.I. Allen, N.R. Velez, R.C. Thayer, N.H. Patel, M.A. Jones, G.F. Meyers, A. M. Minor, Gallium, neon and helium focused ion beam milling of thin films demonstrated for polymeric materials: study of implantation artifacts, *Nanoscale* 11 (3) (2019) 1403–1409, <https://doi.org/10.1039/C8NR08224C>.
- [22] R. Soler, S. Gleich, C. Kirchlechner, C. Scheu, J.M. Schneider, G. Dehm, Fracture toughness of Mo<sub>2</sub>BC thin films: Intrinsic toughness versus system toughening, *Mater. Des.* 154 (2018) 20–27, <https://doi.org/10.1016/j.matdes.2018.05.015>.
- [23] B. Philippi, K. Matoy, J. Zechner, C. Kirchlechner, G. Dehm, Fracture toughness of intermetallic Cu<sub>6</sub>Sn<sub>5</sub> in lead-free solder microelectronics, *Scr. Mater.* 123 (2016) 38–41, <https://doi.org/10.1016/j.scriptamat.2016.05.039>.
- [24] S. Brinckmann, K. Matoy, C. Kirchlechner, G. Dehm, On the influence of microcantilever pre-crack geometries on the apparent fracture toughness of brittle materials, *Acta Mater.* 136 (2017) 281–287, <https://doi.org/10.1016/j.actamat.2017.07.014>.
- [25] R. Danzer, T. Lube, P. Supancic, R. Damani, Fracture of ceramics, *Adv. Eng. Mater.* 10 (4) (2008) 275–298, <https://doi.org/10.1002/adem.200700347>.
- [26] K. Kanaya, K. Adachi, K. Yonehara, Y. Muranaka, H. Ishikawa, Quantitative analysis of knock-on and thermal damage of biological specimens by electron irradiation in transmission electron microscopy, *Micron Microscopica Acta* 22 (3) (1991) 223–237, [https://doi.org/10.1016/0739-6260\(91\)90003-I](https://doi.org/10.1016/0739-6260(91)90003-I).